

Washington University in St. Louis

Washington University Open Scholarship

McKelvey School of Engineering Theses & Dissertations

McKelvey School of Engineering

Spring 5-7-2018

Validation of CFD Simulations for Hypersonic Flow Over a Yawed Cone

Julian Cecil

Washington University in St. Louis

Follow this and additional works at: https://openscholarship.wustl.edu/eng_etds



Part of the [Aerodynamics and Fluid Mechanics Commons](#)

Recommended Citation

Cecil, Julian, "Validation of CFD Simulations for Hypersonic Flow Over a Yawed Cone" (2018). *McKelvey School of Engineering Theses & Dissertations*. 341.

https://openscholarship.wustl.edu/eng_etds/341

This Thesis is brought to you for free and open access by the McKelvey School of Engineering at Washington University Open Scholarship. It has been accepted for inclusion in McKelvey School of Engineering Theses & Dissertations by an authorized administrator of Washington University Open Scholarship. For more information, please contact digital@wumail.wustl.edu.

WASHINGTON UNIVERSITY IN ST. LOUIS
School of Engineering and Applied Science
Department of Mechanical Engineering and Material Science

Thesis Examination Committee:
Ramesh K. Agarwal, Chair
David A. Peters
Swami Karunamoorthy

Validation of CFD Simulations for Hypersonic Flow
Over a Yawed Circular Cone

by
Julian D. Cecil

A thesis presented to the School of Engineering
of Washington University in St. Louis in partial fulfillment of the
requirements for the degree of
Master of Science

May, 2018

Saint Louis, Missouri

© 2018, Julian D. Cecil

Contents

List of Figures	iv
List of Tables	v
Acknowledgments.....	vi
Dedication	vii
Abstract of the Thesis	viii
1 Introduction	1
1.1 Motivation.....	1
1.2 Brief Review of Literature	2
1.3 Scope of the Thesis	2
2 Solution Methodology	3
2.1 Governing Equations.....	3
2.2 Turbulence Modeling.....	3
2.3 Numerical Setup.....	4
2.3.1 Grid Generation.....	4
2.3.2 Solution Algorithm.....	6
2.3.3 Boundary Conditions	7
2.3.4 Convergence Criteria.....	8
3 Results	9
3.1 Test Cases	9
3.2 Simulation Results	9
3.2.1 Cone at 0° and 4° Angle of Attack	13
3.2.2 Cone at 8° Angle of Attack	15
3.2.3 Cone at 12° Angle of Attack.....	17
3.2.4 Cone at 16° Angle of Attack.....	19
3.2.5 Cone at 20° Angle of Attack.....	21
3.3 Grid Independence Study	23
4 Conclusion	25
4.1 Future Work	25

Appendix A	Supplementary Plots	26
A.1	Cone at 4° Angle of Attack	26
A.2	Cone at 8° Angle of Attack	28
A.3	Cone at 12° Angle of Attack	29
A.4	Cone at 16° Angle of Attack	31
A.5	Cone at 20° Angle of Attack	32
Appendix B	Computer Specifications.....	34
References		35
Vita		37

List of Figures

Figure 1: Isometric View of the Computational Domain.....	4
Figure 2: Top and Side Views of the Computational Domain Around the Cone.....	5
Figure 3: Top and Side Views of Fluent Mesh	6
Figure 4: Rear View of Fluent Mesh Showing the Outlet Plane.....	6
Figure 5: Surface Pressure on the Cone for Six Yaw Angles.....	10
Figure 6: Details for Surface Pressure on the cone for Six Yaw Angles	11
Figure 7: Normalized Local Heat Transfer on the Cone for Six Yaw Angles.....	12
Figure 8: Surface Pressure on the Cone at 0° and 4° Yaw.....	13
Figure 9: Normalized Local Heat Transfer Coefficient on the Cone at 0° and 4° Yaw.....	14
Figure 10: Surface Pressure on the Cone at 8° Yaw	15
Figure 11: Normalized Local Heat Transfer Coefficient on the Cone at 8° Yaw	11
Figure 12: Surface Pressure on the Cone at 12° Yaw	17
Figure 13: Normalized Local Heat Transfer Coefficient on the Cone at 12° Yaw	18
Figure 14: Surface Pressure on the Cone at 16° Yaw	19
Figure 15: Normalized Local Heat Transfer Coefficient on the Cone at 16° Yaw	20
Figure 16: Surface Pressure on the Cone at 20° Yaw	21
Figure 17: Normalized Local Heat Transfer Coefficient on the Cone at 20° Yaw	22
Figure 18: Computed Surface Pressure on the Cone at 4° yaw angle for four grid densities ranging from 2.3 million to 7.1 million cells	23
Figure 19: Computed normalized Heat Transfer Coefficient on the cone at 4° yaw angle for four grid densities ranging from 2.3 million to 7.1 million cells	24

List of Tables

Table 1: Freestream Conditions	7
Table 2: Computer Hardware Used in Simulations	34

Acknowledgments

I would like to extend my deepest appreciation to my advisor, Ramesh Agarwal, for supporting me and providing guidance in this research project. I would not have been able to do it without him. I want to thank my colleagues Junhui Li and James Mitchell for helping me in learning the ANSYS Fluent and ICEM CFD software packages. I also want to thank my parents for the financial and emotional support. Finally, I want to thank my friends of the Wash-U Racing team for providing the resources that made this project possible.

Julian D. Cecil

Washington University in St. Louis

May 2018

Dedicated to my Brother, Lane.

ABSTRACT OF THE THESIS

Validation of CFD Simulations for Hypersonic Flow over a Yawed Circular Cone

by

Julian D. Cecil

Master of Aerospace Engineering

Washington University in St. Louis, 2018

Research Advisor: Ramesh K. Agarwal, PhD

This study aims to numerically simulate the wind tunnel results for hypersonic flow over a circular cone of semi-apex angle of 10 degrees yawed from 0° to 20° using the commercial computational fluid dynamics software ANSYS Fluent. The ANSYS workbench is used to create the 10° semi-apex circular cone with a shock aligned structured mesh of 3.05 million cells surrounding the cone. Simulation boundary conditions for pressure and temperature in the far field correspond to Tracy's wind tunnel experiment at Cal Tech. The six simulation cases are conducted for yaw angles of 0, 8, 12, 16, 20 and 24 degrees. The unsteady Reynolds-Averaged compressible Navier-Stokes solver with Spalart-Allmaras (SA) turbulence model is employed. The upstream flow Mach number is $M = 8$ and Reynolds number is $Re_\infty = 4.2 \times 10^5$ based on cone generator length. The maximum variation in static pressure computations around the cone is 7% of the experimental values and the maximum variation in heat transfer computations is within 12% of the experimental values; the maximum difference between the computations and experiment occurs at the leeward meridian of the cone. By further refinement of the mesh and using other turbulence models, it is possible that computational accuracy of the simulations may be further improved; however it requires additional investigation. Nevertheless the present simulations demonstrate that CFD can be employed with sufficient accuracy to compute the hypersonic flows about space vehicles with fully turbulent flow.

Chapter 1

Introduction

1.1 Motivation

Space vehicles for hypersonic flight have been designed in the past using a variety of methods such as wind tunnel testing, aerodynamic theory, and full-scale field testing. The conditions present in hypersonic flow are difficult to fully capture due to ionization, extreme friction heating with high temperatures, and chemical reactions. Wind tunnel testing can accurately replicate some of these conditions for a scale model. However, test sections for hypersonic tunnels are limited in size, require vast amounts of power, and can only isolate one flow variable at a time. Thus, wind tunnel testing does not facilitate rapid design changes. Purely mathematical models are limited in practice due to many simplifying assumptions needed to obtain a solution. These models often do not produce a closed form solution and are often limited to either axisymmetric or simple geometries. In many cases, a very simplified model is not accurate enough to describe the conditions present in real hypersonic flows. Numerical analysis using computational fluid dynamics (CFD) technology, has become more popular over the past few decades as a cost effective, yet acceptably accurate approach to analyze the hypersonic aerodynamics. Computer simulations are appealing since they support rapid design changes and allow for computation of the flow field about complex geometries. They also include models for describing the real gas effects and turbulence. However, CFD methods are not perfect either: they are heavily dependent on boundary conditions and grid quality and can produce widely varying results. This study aims to validate CFD simulations against established experimental results for hypersonic flow past yawed cones to develop best practice guidelines that can be used for modeling hypersonic flows.

1.2 Brief Review of Literature

Hypersonic flow past cones has been a subject of study for more than 60 years. Tables for symmetrical hypersonic flow such as Bartlett's [1] and yawed hypersonic flow such as Kopal's [2] have been generated using various mathematical approximating models. Ferri [3] has shown that the first order theory for supersonic flow over a circular cone matches well with the experimental data even up to 12° yaw. Hypersonic flow past yawed cones was further examined by Sapunkov [4], who obtained solutions for the flow field between the shock and the cone surface. His method however had singularities at the surface and thus was inapplicable close to the cone surface. In the past few decades, CFD has been employed extensively for analyzing the hypersonic flows over conical geometries and other space vehicles. Moss, LaBeau, and Glass [5] examined the Mach 10 flow in a low-density wind tunnel over a sharp double cone using the direct simulation Monte Carlo (DSMC) method. They found a particular sensitivity in the solver to grid resolution. Gosse and Kimmel [6] conducted Mach 8 simulations over an elliptic cone with good agreement between CFD and experiment.

1.3 Scope of the Thesis

The goal of this thesis is to use the wind tunnel experiment results published in 1963 by Richard R. Tracy [7] for validation of CFD methodology for computing hypersonic flows employing the commercially available CFD software, ANSYS Fluent. Tracy obtained the experimental data for Mach 8 flow over a sharp circular cone at different yaw angles and six different Reynolds numbers. His experimental data includes surface pressure and heat transfer measurements at two locations on the cone. The CFD simulations in this thesis are performed for six yaw angles and at flow conditions of free-stream pressure 259.3 psia, free-stream temperature 1360 °R, and Reynolds number $Re = 4.2 \times 10^5$. Surface pressure and heat transfer data extracted from the simulations are compared against the experimental data.

Chapter 2

Solution Methodology

2.1 Governing Equations

The Reynolds-Averaged Navier-Stokes (RANS) equations in conjunction with a turbulence model are used to compute the compressible turbulent flow fields of hypersonic flow past yawed cones. The conservation equations of mass, momentum (RANS equations), and energy along with the equation of state for an ideal gas are solved for the six flow variables – pressure, density, temperature, and three components of velocity. These equations are solved using the commercial CFD solver Fluent.

2.2 Turbulence Modeling

This study employs the one-equation Spalart-Allmaras (SA) model for modeling the “Reynolds Stresses” in the RANS equations. The SA model was designed especially for aerodynamic flows and solves a modelled transport equation for the turbulent eddy viscosity. It has been found to be reasonably accurate for a wide variety of aerodynamic flows in subsonic and transonic regimes. It may not be quite accurate for computing hypersonic turbulent flows; the goal of this research is to assess its accuracy for computing hypersonic flows.

2.3 Numerical Setup

2.3.1 Grid Generation

The circular cone's dimensions were obtained directly from Tracy's [7] experimental configuration. A bilateral symmetry plane was used to cut the model in half, extending from the windward meridian to the leeward meridian. The computational domain is bounded by the symmetry plane, the cone surface, an outlet plane, and a far field boundary. Figure 1 shows an isometric view of the computational domain.

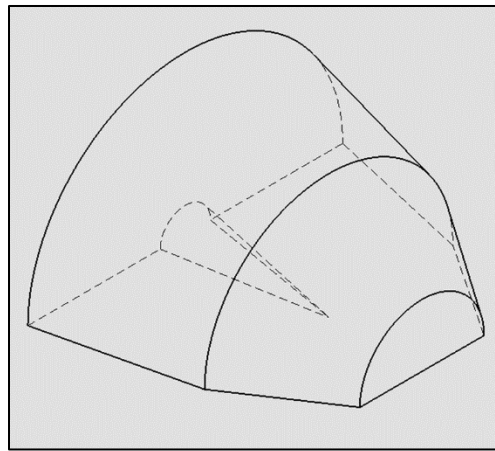


Figure 1: Isometric View of the Computational Domain

The far field surface of the computational domain is a segmented frustum with diameters 4.0 inches at the inlet, 8 inches at the segment, and 10.14 inches at the outlet. The outer diameter is 6.0 times greater than the diameter of the cone surface and is sufficiently large to capture the shock cone at the largest angle of attack. A conical mesh was chosen instead of a rectangular mesh since it projects more accurately on the round cone surface and requires 50.5% less computational domain size. This serves to increase the computational efficiency and decrease the simulation time. Figure 2 shows a top down view of the computational domain, looking at the symmetry plane and a cross sectional view showing the cone dimensions. The cone apex is truncated to a very small diameter of 0.002 inches, which is the machining tolerance specified in Tracy's experimental model. This was done to increase the quality of the mesh and avoid the meshing problems frequently encountered with a sharp tip.

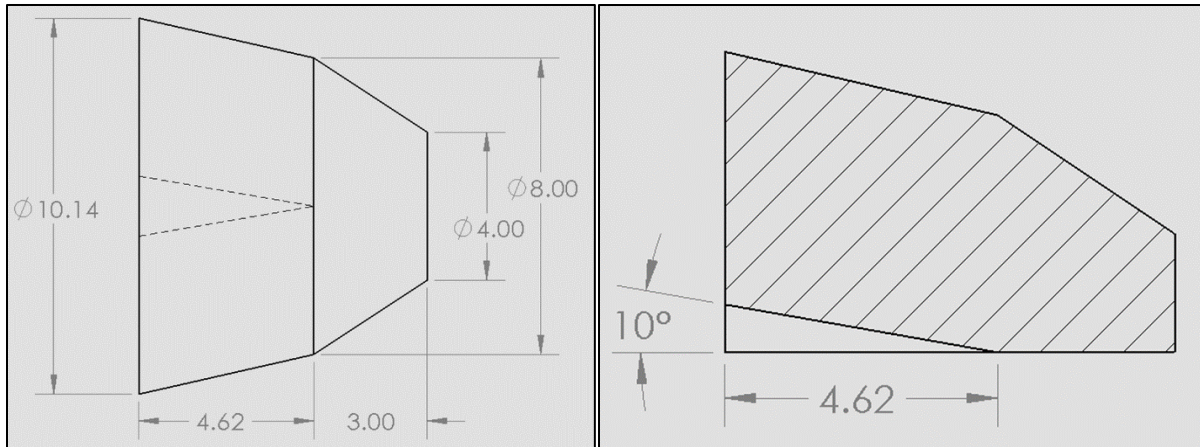


Figure 2: Top and Side Views of the Computational Domain Around the Cone

The cone's shock angle was calculated using Taylor-Maccoll analysis [8]. At Mach 8 and semi-apex cone angle of 10 degrees, the shock angle is 13.05 degrees. The grid is aligned such that the mesh elements near the cone surface are nearly parallel to the surface for boundary layer resolution, and elements near the shock are parallel to a cone angle of 13.05 degrees for shock layer resolution.

The radial direction has 100 elements starting in size from 9×10^{-6} inches at the cone surface and growing outward with a ratio of 1.2. This places 5 elements inside the boundary layer, calculated for a y^+ of 1.0, for adequate resolution of the turbulent boundary layers [9]. The circumferential direction has 135 uniformly spaced elements, and the lengthwise direction has 120 elements starting at 9×10^{-6} inches at the cone tip, growing outward with a ratio of 1.2 for smooth transition with the far field mesh elements. The remaining mesh dimensions were adjusted until the overall mesh quality was greater than 0.7. The resulting truncated conical mesh has 3.05 million volume elements. Figure 3 shows the top and side views of the resulting grid. The purple surface is the symmetry plane, seen in the top view, and the red surface is the far field boundary. The interior green area is the cone surface. Figure 4 shows a rear view of the computational domain (outlet boundary plane). The elements along the circumference have an angular resolution of 1.33 degrees per cell.

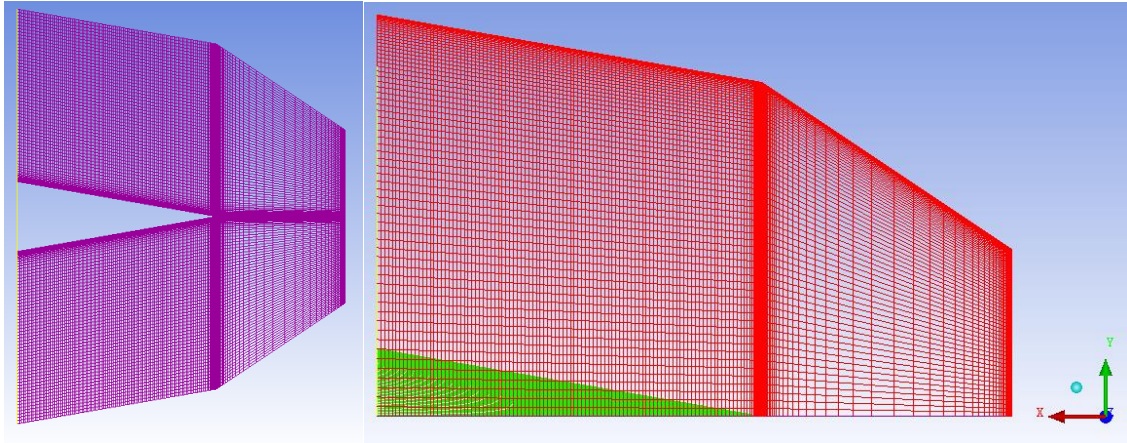


Figure 3: Top and Side Views of Fluent Mesh

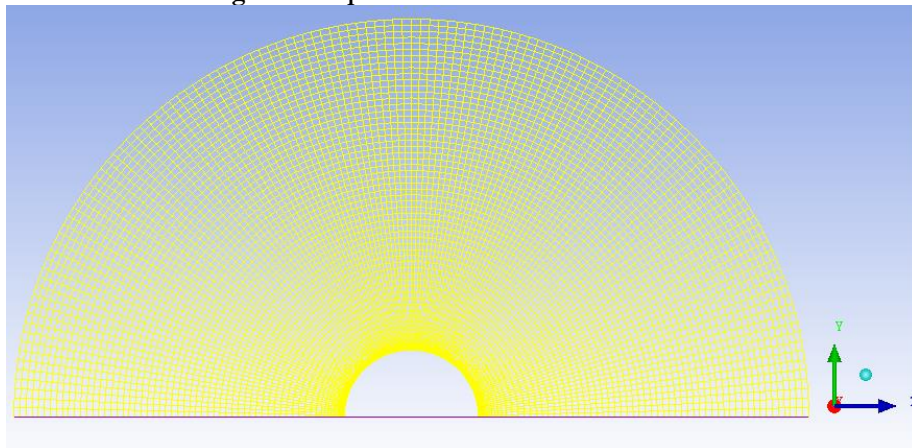


Figure 4: Rear View of Fluent Mesh Showing the Outlet Plane

2.3.2 Solution Algorithm

A double precision implicit solver, using the Advection Upstream Splitting Method (AUSM) is used in all simulations. The gradients are calculated with the least squares cell-based gradient method. A second order upwind scheme is used for discretization of both the RANS and SA turbulence equations. Sutherland's viscosity law [10] is used to account for the high temperature effects on the molecular viscosity.

2.3.3 Boundary Conditions

The computational domain has four bounding surfaces, one each for the far field, symmetry plane, outlet plane, and the cone surface. Isentropic flow relations are used to calculate the static pressure and static temperature from the given total pressure and total temperature [11]. These relations are shown below in Eq. (2.1) and Eq. (2.2).

$$\frac{p}{p_t} = \left(1 + \frac{\gamma-1}{2} M^2\right)^{-\frac{\gamma}{\gamma-1}} \quad (2.1)$$

$$\frac{T}{T_t} = \left(1 + \frac{\gamma-1}{2} M^2\right)^{-1} \quad (2.2)$$

At Mach 8, for 1.788 MPa total pressure and 755.6 K total temperature, the static pressure is 190.7 Pa and the static temperature is 55.4 K. The static flow variable conditions are used in Fluent to specify the far field as a pressure-inlet. Tracy mentions that the cone is actively cooled such that the wall temperature to freestream total temperature ratio is 0.40. The cone surface is a smooth copper wall at constant temperature of 302.2 K. The outlet boundary condition is specified as a pressure-outlet condition. Table 1 summarizes the freestream quantities.

Table 1: Freestream Conditions

M_∞	7.95
$p_{t\infty}$ (MPa)	1.788
$T_{t\infty}$ (K)	755.6
p_∞ (Pa)	190.98
T_∞ (K)	55.39
T_w (K)	302.2 K

Sutherland's law of viscosity, given in Eq. (2.3), is used because it is more accurate considering the large temperature difference between the far field (55 K) and the cone surface (302 K) [10].

$$\mu = \mu_{ref} \left(\frac{T}{T_{ref}} \right)^{3/2} \frac{T_{ref} + S}{T + S} \quad (2.3)$$

2.3.4 Convergence Criteria

Five convergence criteria are used to determine the convergence of the solution. Numerical residuals for the six conservation equations must be below 10^{-6} for the solution to be considered converged. Surface integrals over the cone for both static pressure and heat transfer coefficient are monitored. These values should not change between iterations for the solution to be considered converged. Finally, mass and heat fluxes through each of the four surfaces are monitored to assure the system's adherence to conservation laws. The sum of the fluxes must be zero for the solution to be converged.

Chapter 3

Results

3.1 Test Cases

Six simulation cases are computed for the cone yaw angles of 0, 4, 8, 12, 16, and 20 degrees. The nondimensional pressure and nondimensional heat transfer coefficient are calculated to compare them with the experimental data of Tracy [7]. The nondimensional pressure is defined as a ratio of the static pressure to free stream total pressure, and the nondimensional heat transfer coefficient is defined as a ratio of the yawed heat transfer coefficient to un-yawed heat transfer coefficient. This study considers only the first set of Tracy's experiment with 259.3 psia supply pressure, 1360 °R supply temperature, and freestream Reynolds number of 4.2×10^6 . Following Tracy's experiment, computational values are also obtained 4.0 inches from the vertex of the cone.

3.2 Simulation Results

Figure 5 shows the comparison of computed and experimental variables of surface pressure coefficient on the cone from windward side ($\varphi = 0^\circ$) to leeward side ($\varphi = 180^\circ$) for the six yawed angles. All the computations are performed with 3.05 million grid points, except for the case of the cone at zero angle of attack. Excellent agreement between the computations and experimental data can be observed. Figure 6 shows the details of the pressure distributions in the ranges $\varphi = 90^\circ$ to 180° . Some disagreement can be seen between the computational experiment at yaw angles $\alpha = 16^\circ$ and 20° .

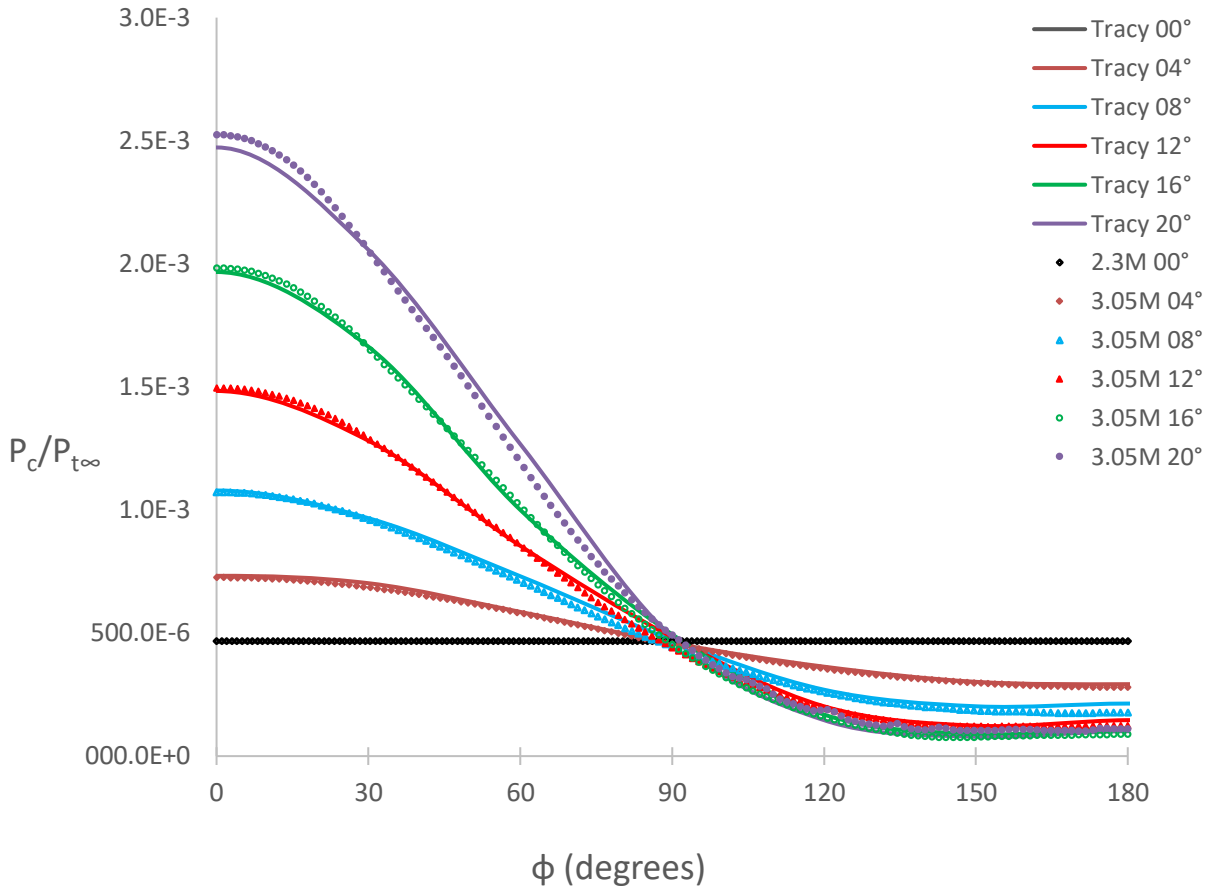


Figure 5: Surface Pressure on the Cone for Six Yaw Angles

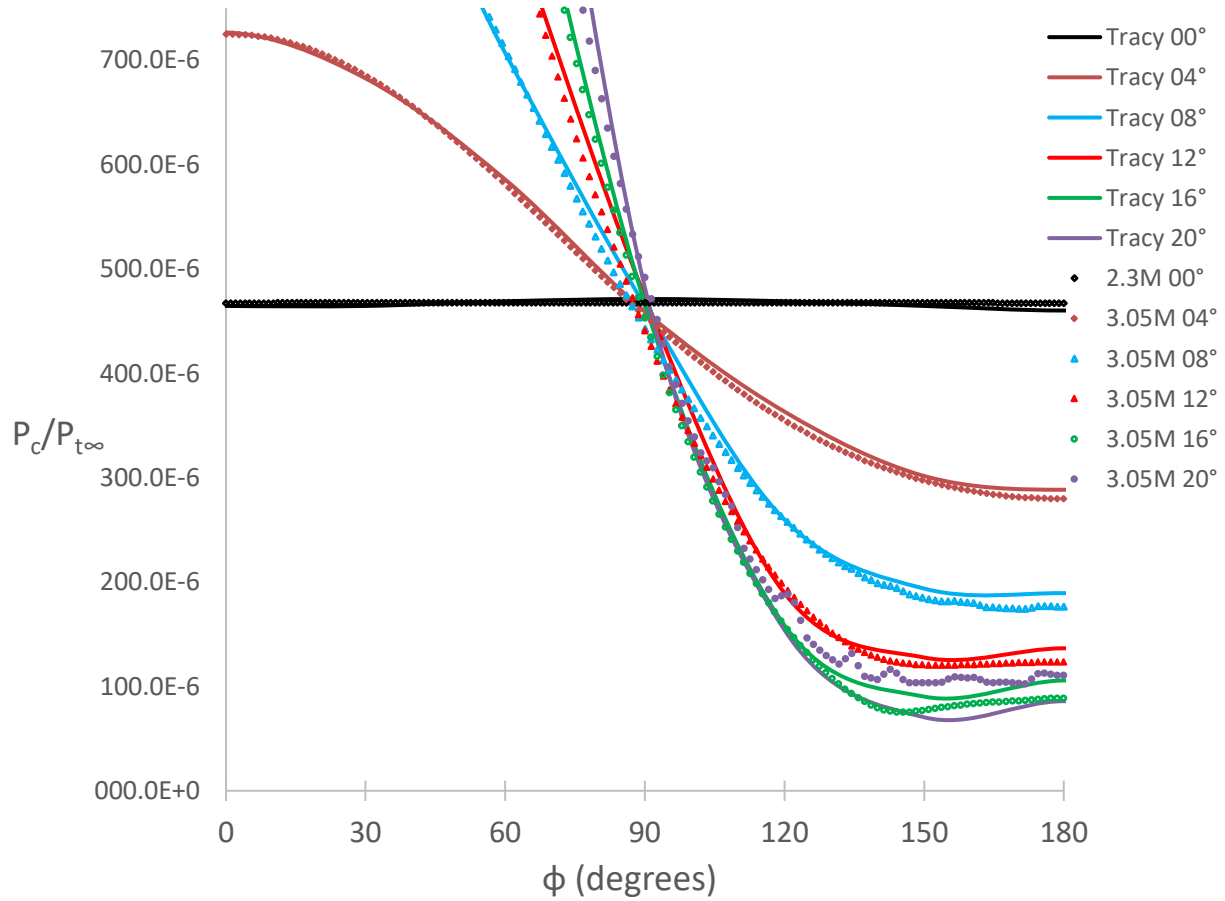


Figure 6: Details for Surface Pressure on the cone for Six Yaw Angles

Figure 7 shows the comparison of the computed and experimental normalized local heat transfer on the cone from the windward side ($\varphi = 0^\circ$) to the leeward side ($\varphi = 180^\circ$) for the six yawed angles. All the computations are performed with 3.05 million grid points except the case of the cone at zero angle of attack performed with 2.3 million grid points. It can be seen that the disagreement between the computations and experimental data increases from $\varphi = 90^\circ$ to $\varphi = 180^\circ$ on the leeward side and also with increase in angle of attack. This can be attributed to lack of enough grid points near the surface and/or to the SA turbulence model. Based on the grid independence study reported later in the thesis, it is surmised that this disagreement can more likely be attributed to the SA model which is really not appropriate for high speed flows.

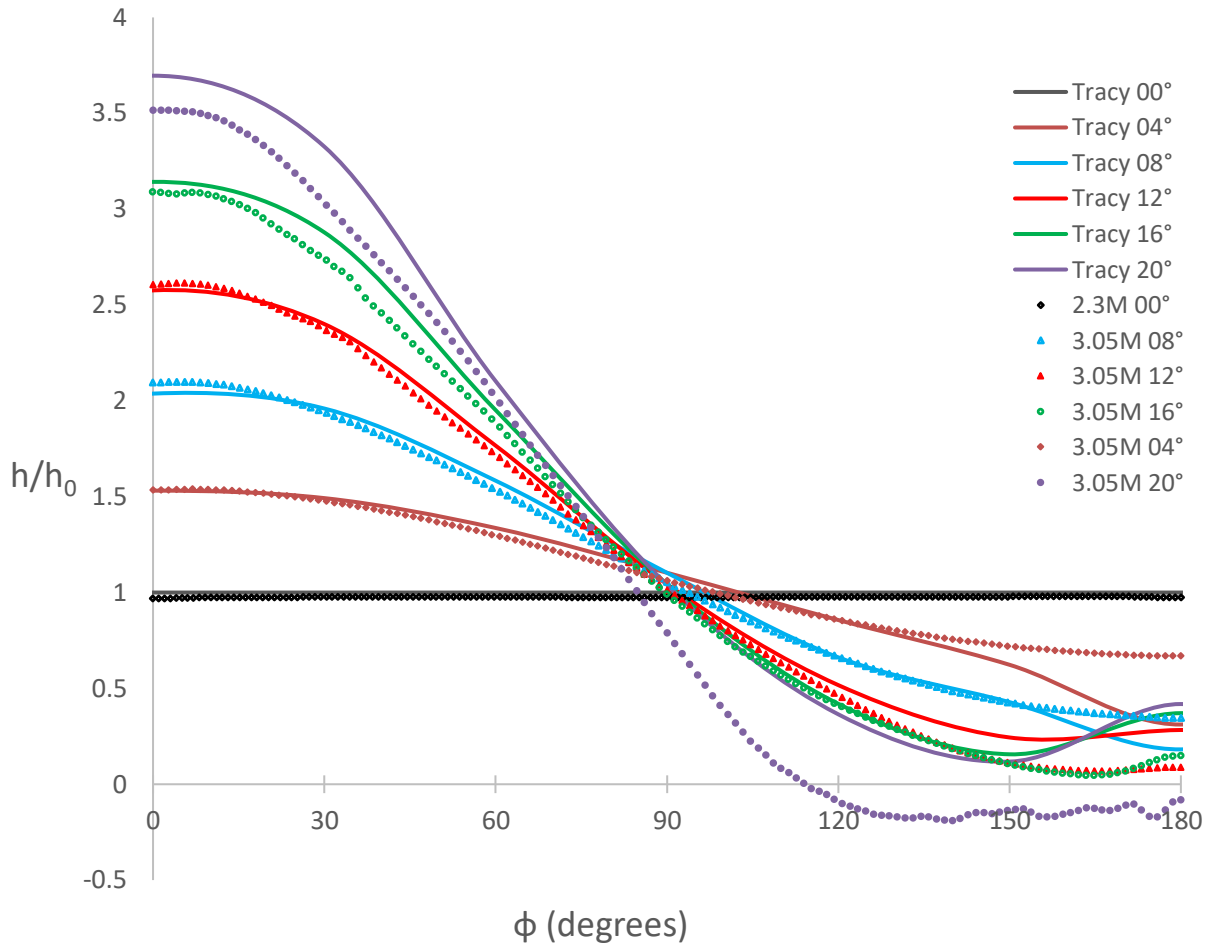


Figure 7: Normalized Local Heat Transfer on the Cone for Six Yaw Angles

In the following subsections, more clear graphs for comparison of computed pressure and experimental data for static pressure and heat transfer on the cone are presented at various angles of yaw.

3.2.1 Cone at 0° and 4° Angle of Attack

Figure 8 and 9 show the surface pressure and heat transfer on the cone surface for 0° and 4° angles of attack. It can be seen from Figure 8 that the computed and experimental pressure distributions are in reasonably good agreement. However, Figure 9 shows that there is large discrepancy between the computed and experimental heat transfer coefficient for $\varphi = 90^\circ$ to 180° . Based on the grid independence study it is conjectured that this discrepancy is likely due to the use of the SA turbulence model which is really not suitable for high speed flows.

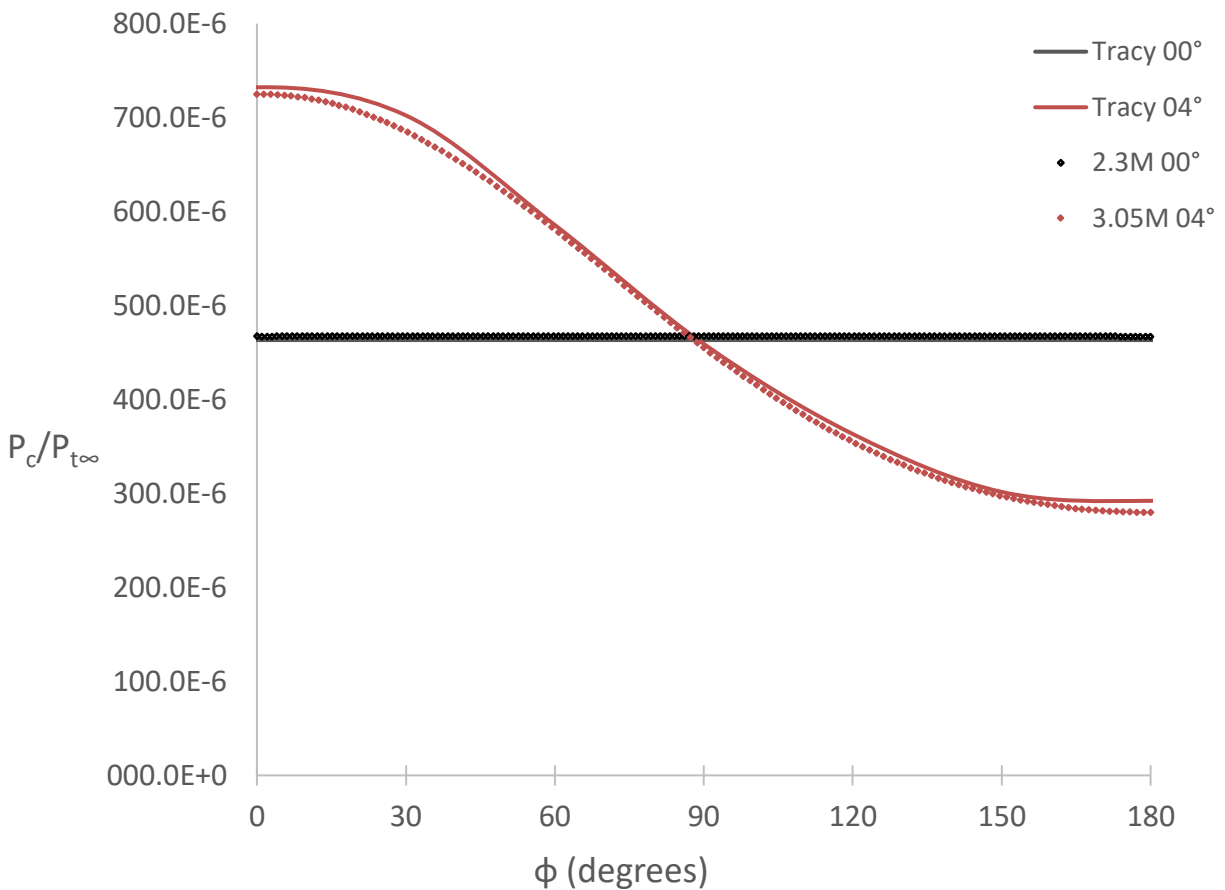


Figure 8: Surface Pressure on the Cone at 0° and 4° Yaw

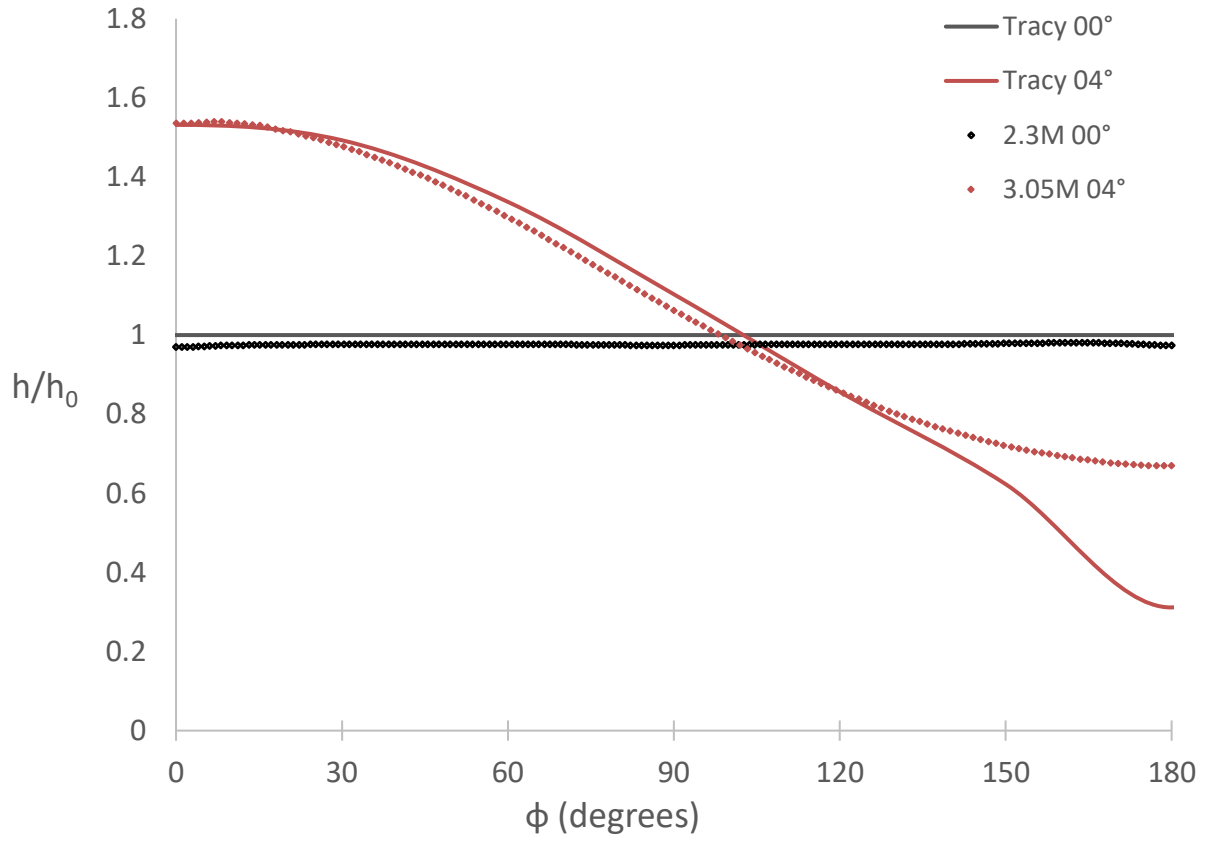


Figure 9: Normalized Local Heat Transfer Coefficient on the Cone at 0° and 4° Yaw

3.2.2 Cone at 8° Angle of Attack

Figures 10 and 11 show the surface pressure and heat transfer on the cone surface for 8° angle of attack. It can be seen from Figure 10 that the computed and experimental pressure distributions are in reasonably good agreement. However, Figure 11 shows that there is large discrepancy between the computed and experimental heat transfer coefficient for $\varphi = 90^\circ$ to 180° . Based on the grid independence study it is conjectured that this discrepancy is likely due to the use of the SA turbulence model which is really not suitable for high speed flows.

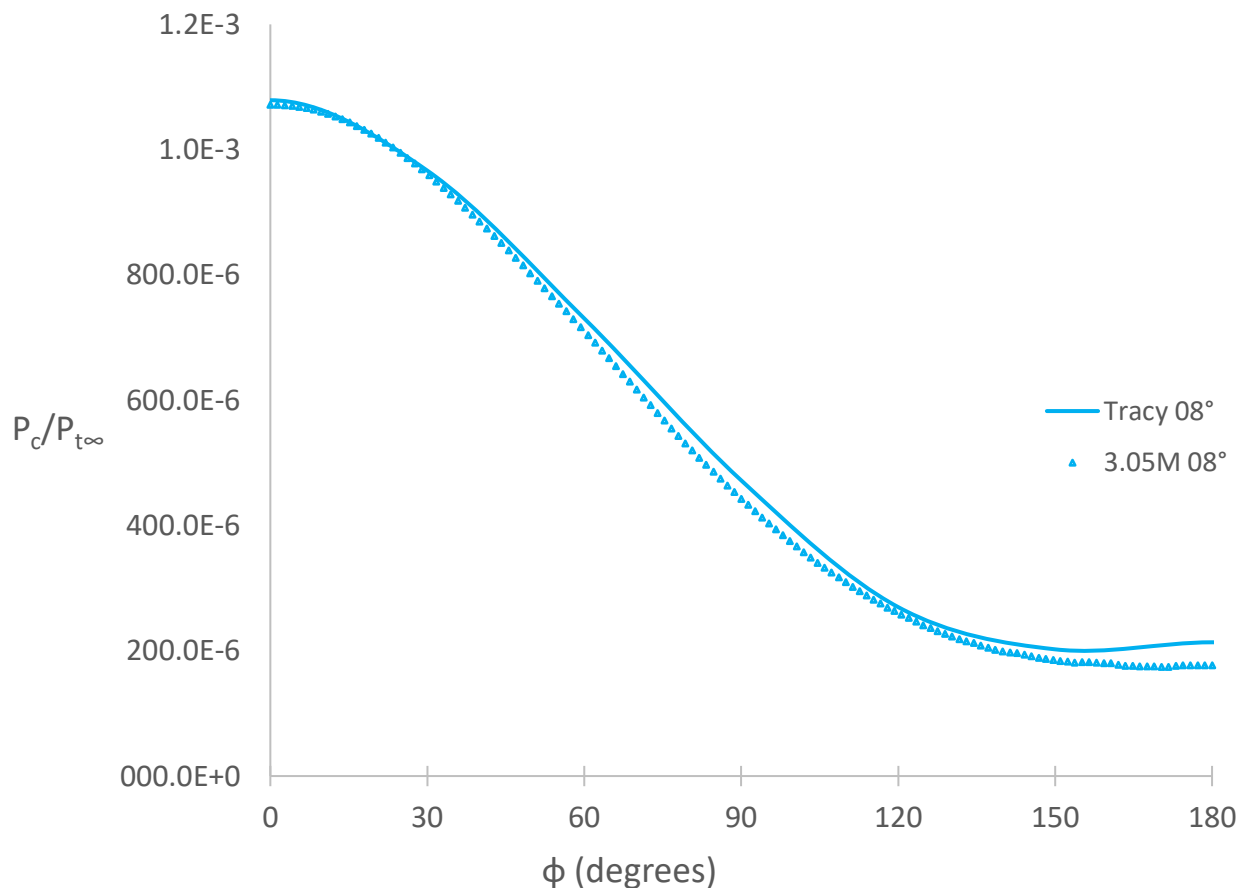


Figure 10: Surface Pressure on the Cone at 8° Yaw

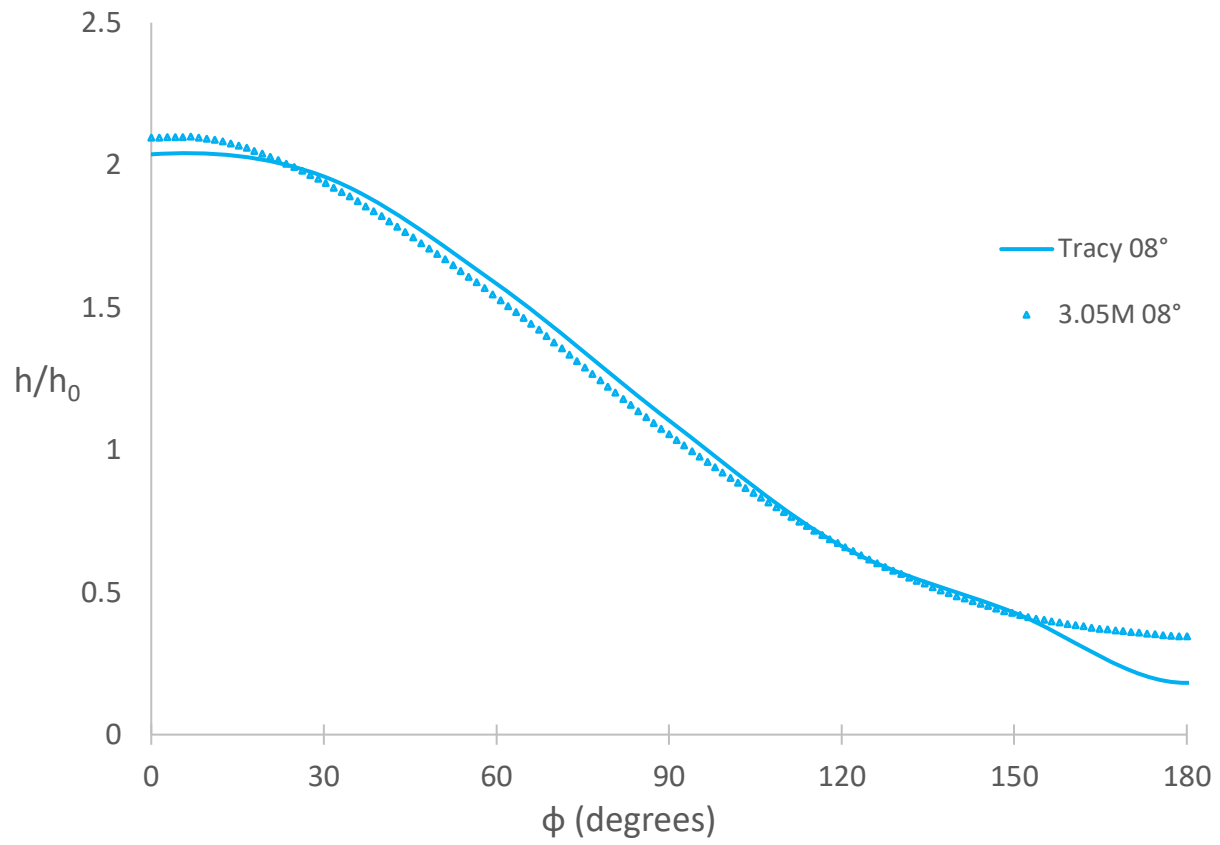


Figure 11: Normalized Local Heat Transfer Coefficient on the Cone at 8° Yaw

3.2.3 Cone at 12° Angle of Attack

Figures 12 and 13 show the surface pressure and heat transfer on the cone surface for 12° angle of attack. It can be seen from Figure 12 that the computed and experimental pressure distributions are in reasonably good agreement. However, Figure 13 shows that there is large discrepancy between the computed and experimental heat transfer coefficient for $\varphi = 90^\circ$ to 180° . Based on the grid independence study it is conjectured that this discrepancy is likely due to the use of the SA turbulence model which is really not suitable for high speed flows.

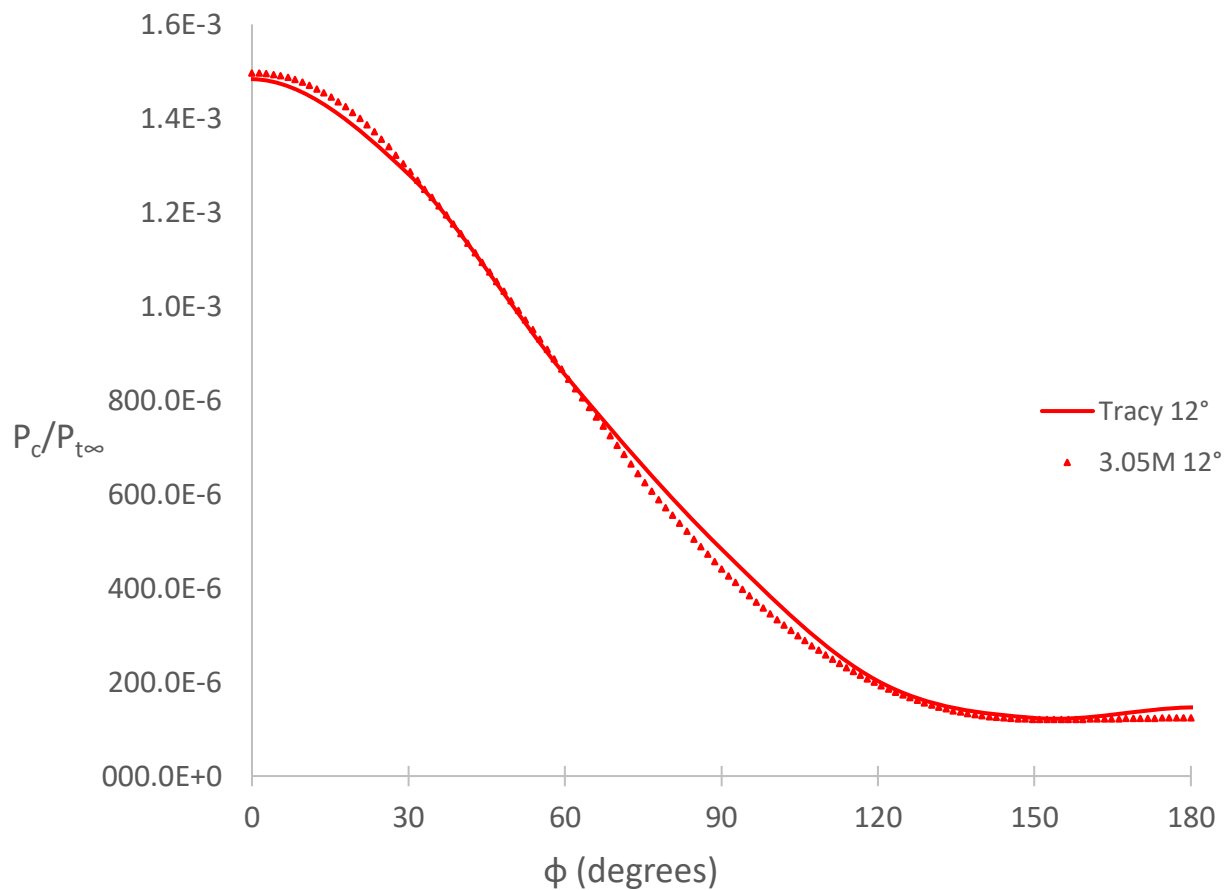


Figure 12: Surface Pressure on the Cone at 12° Yaw

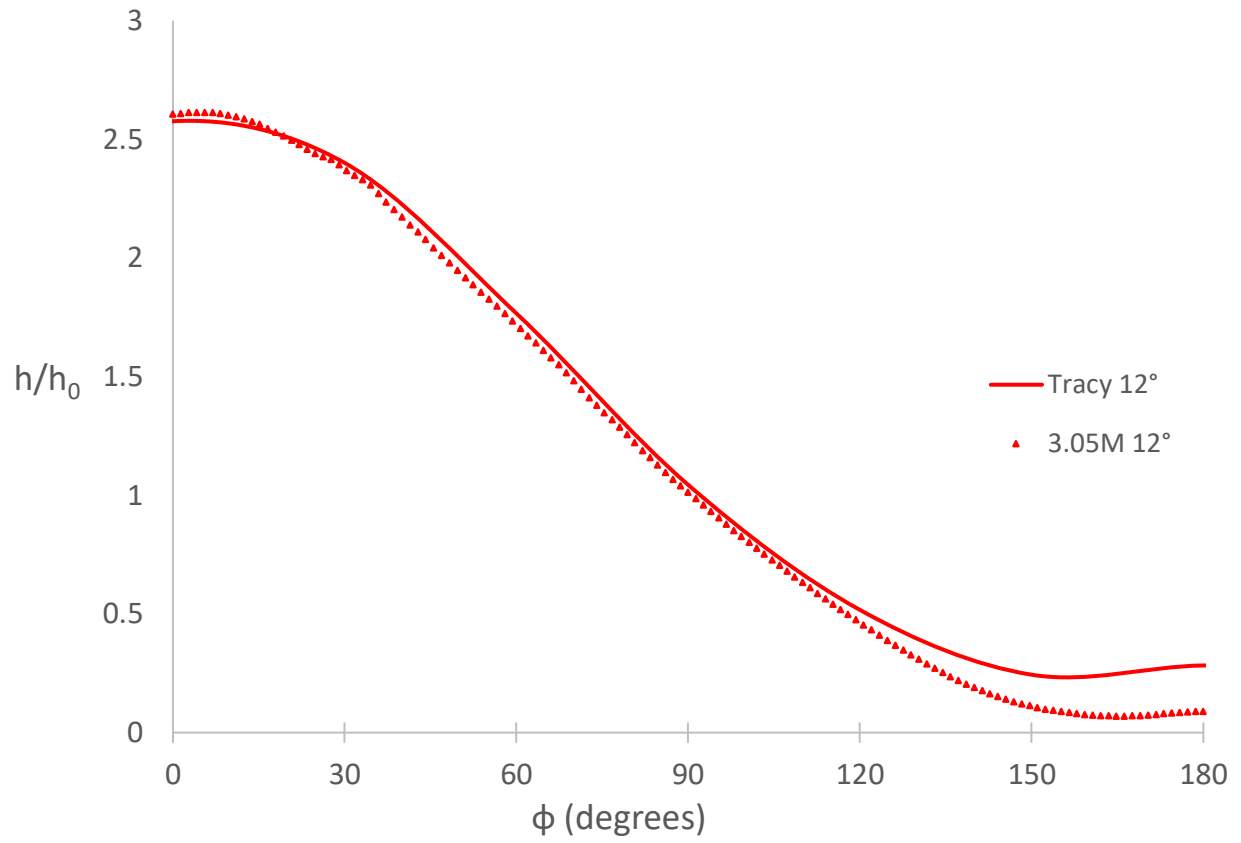


Figure 13: Normalized Local Heat Transfer Coefficient on the Cone at 12° Yaw

3.2.4 Cone at 16° Angle of Attack

Figures 14 and 15 show the surface pressure and heat transfer on the cone surface for 16° angle of attack. It can be seen from Figure 14 that the computed and experimental pressure distributions are in reasonably good agreement. However, Figure 15 shows that there is large discrepancy between the computed and experimental heat transfer coefficient for $\varphi = 90^\circ$ to 180° . Based on the grid independence study it is conjectured that this discrepancy is likely due to the use of the SA turbulence model which is really not suitable for high speed flows.

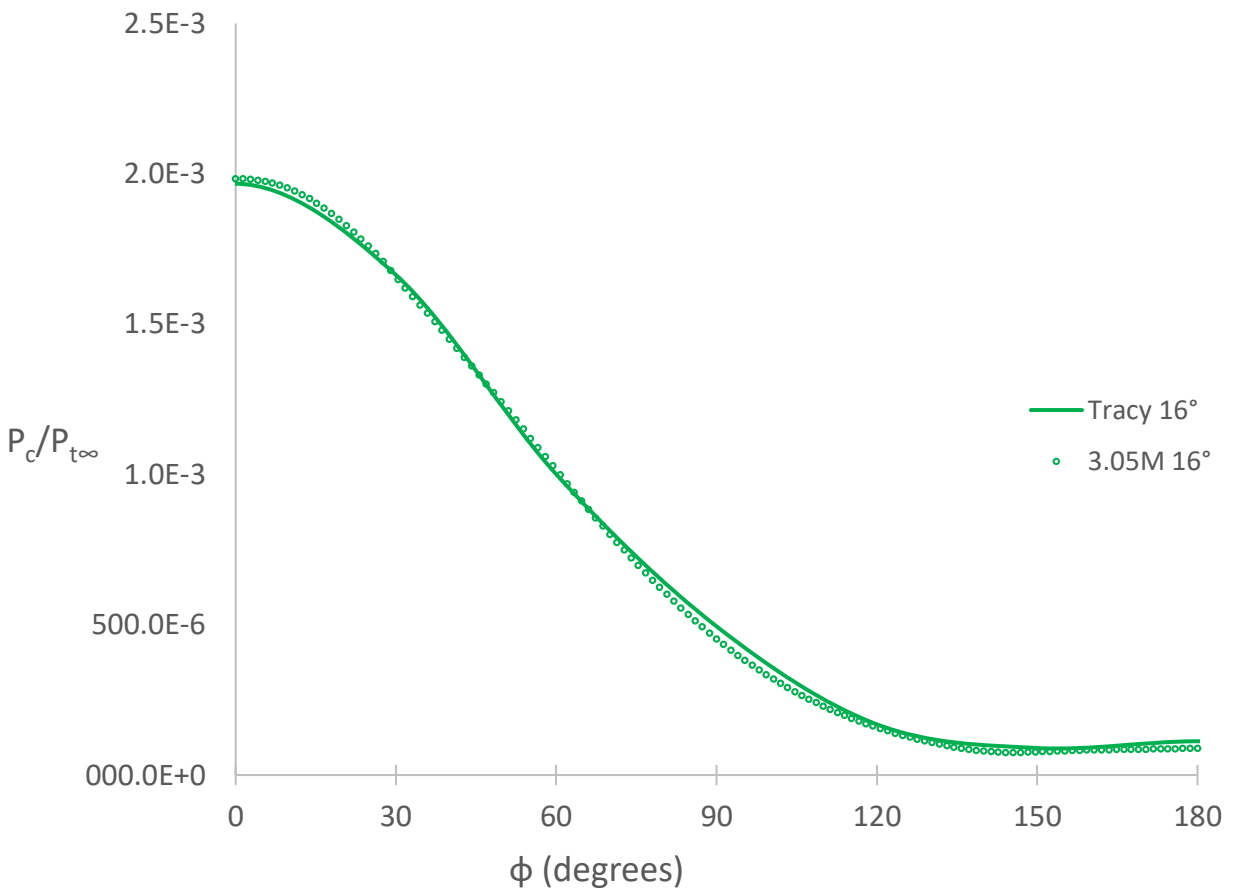


Figure 14: Surface Pressure on the Cone at 16° Yaw

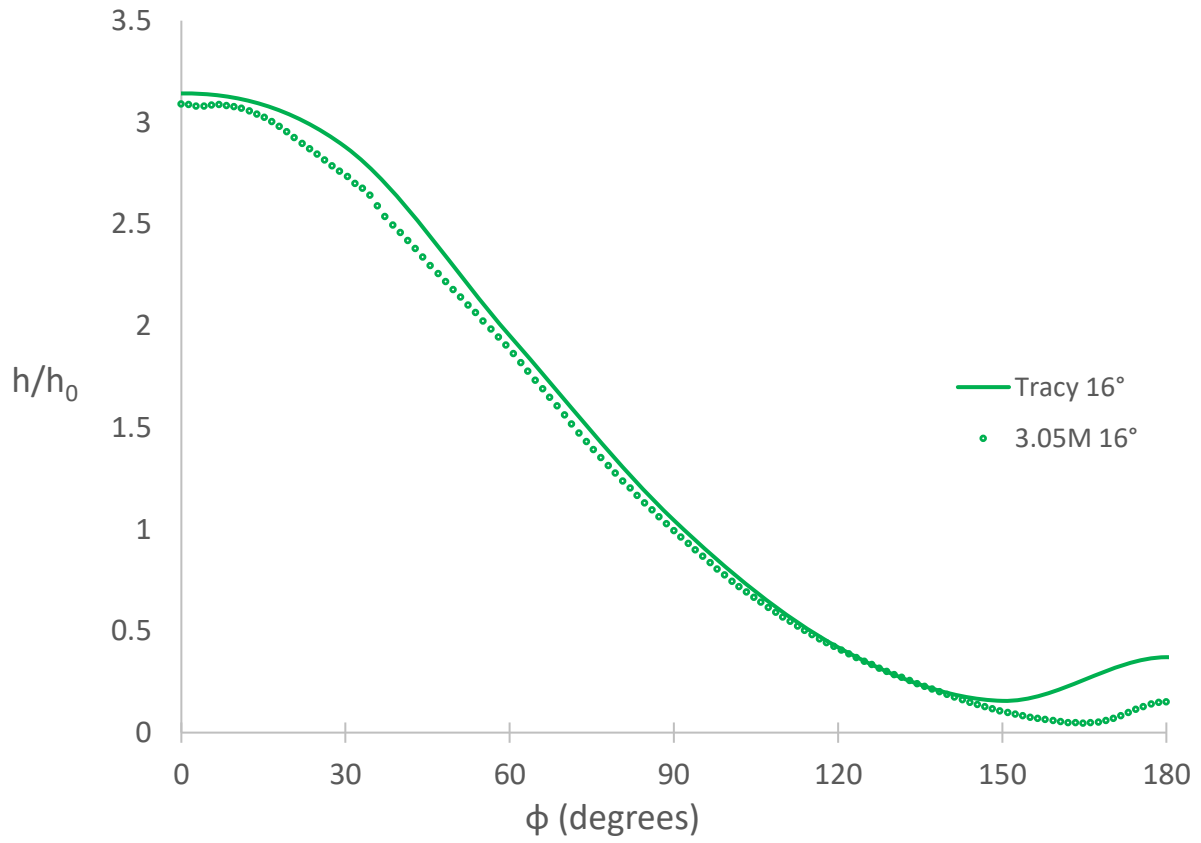


Figure 15: Normalized Local Heat Transfer Coefficient on the Cone at 16° Yaw

3.2.5 Cone at 20° Angle of Attack

Figures 16 and 17 show the surface pressure and heat transfer on the cone surface for 20° angle of attack. It can be seen from Figure 16 that the computed and experimental pressure distributions are in reasonably good agreement. However, Figure 17 shows that there is large discrepancy between the computed and experimental heat transfer coefficient for $\varphi = 90^\circ$ to 180° . Based on the grid independence study it is conjectured that this discrepancy is likely due to the use of the SA turbulence model which is really not suitable for high speed flows.

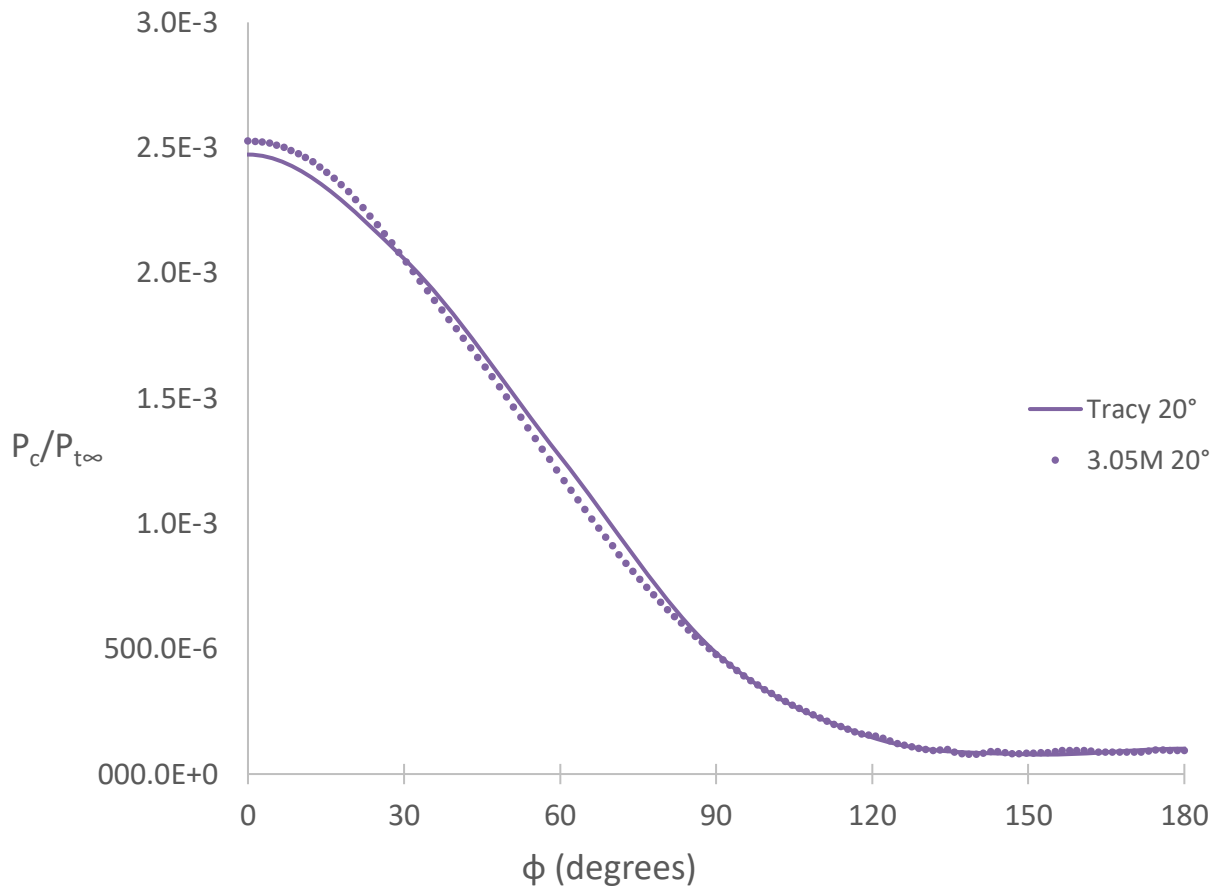


Figure 16: Surface Pressure on the Cone at 20° Yaw

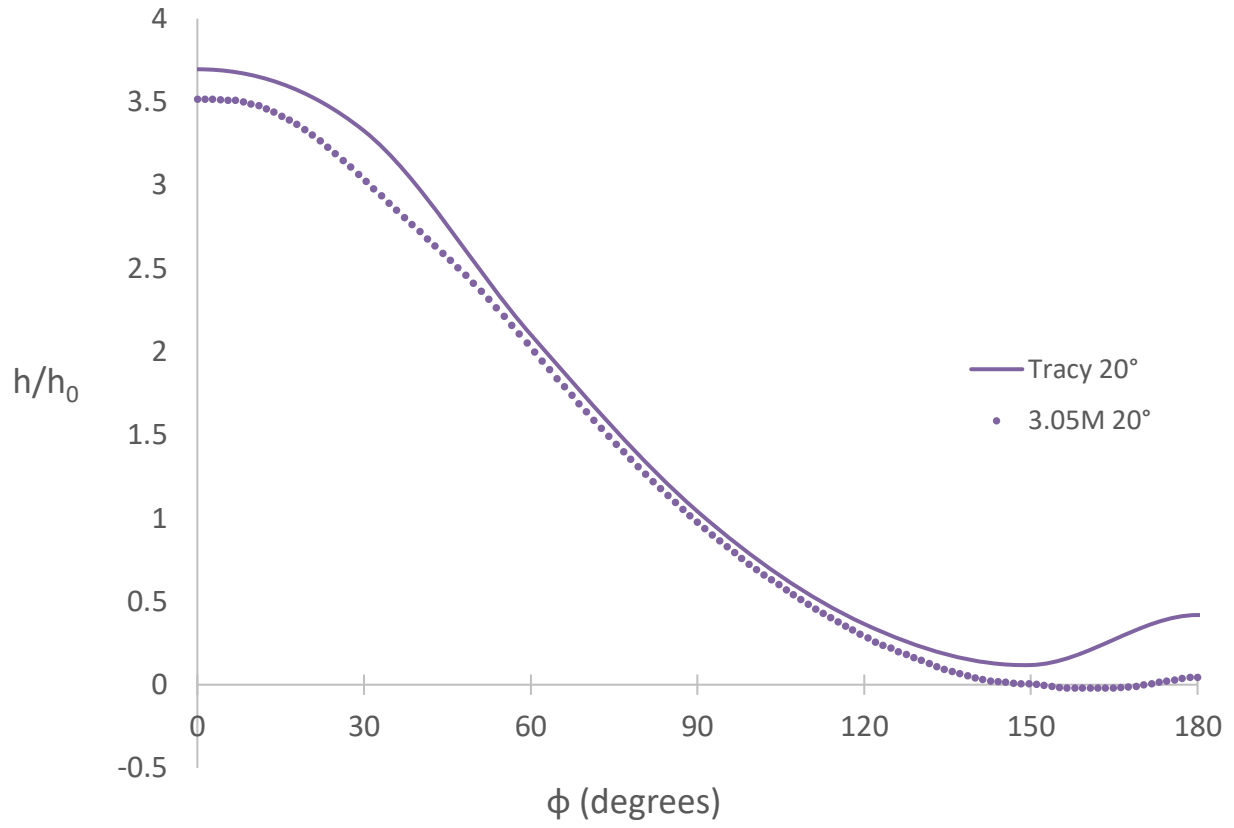


Figure 17: Normalized Local Heat Transfer Coefficient on the Cone at 20° Yaw

3.3 Grid Independence Study

Figures 18 and 19 show the simulation results for the cone at 4° yaw with identical upstream flow conditions for 4 different grid sizes. The results shown are at 2.3 million, 3.05 million, 5.4 million, and 7.1 million grid points.

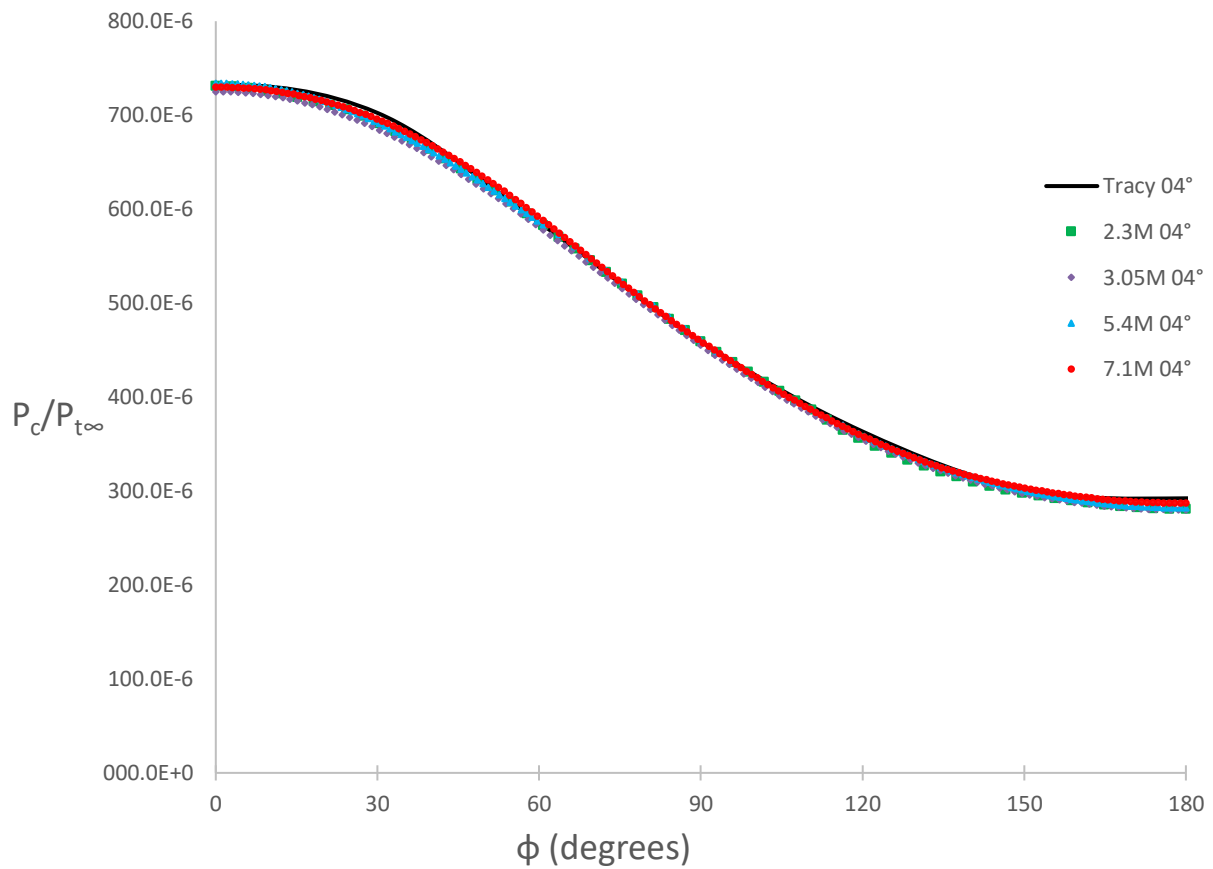


Figure 18: Computed Surface Pressure on the Cone at 4° yaw angle for four grid densities ranging from 2.3 million to 7.1 million cells

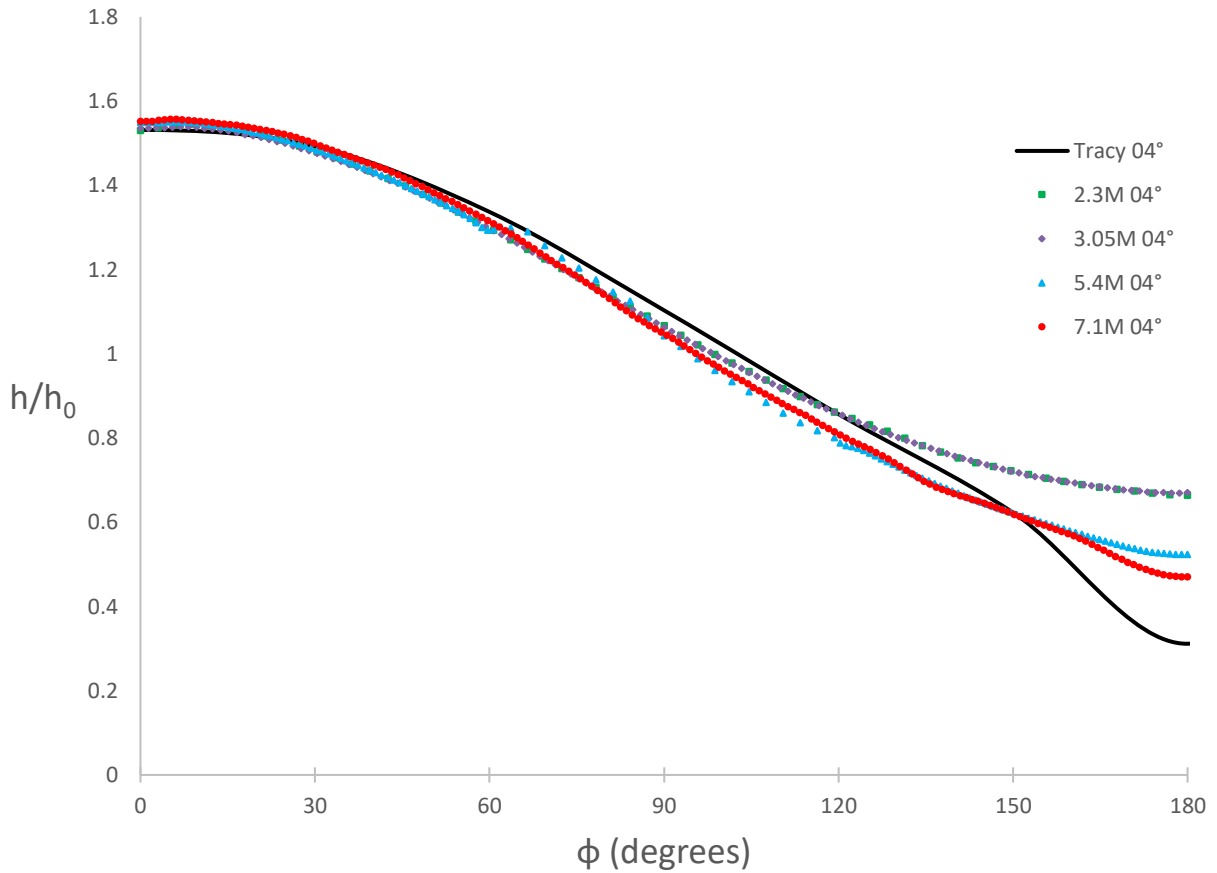


Figure 19: Computed normalized Heat Transfer Coefficient on the cone at 4° yaw angle for four grid densities ranging from 2.3 million to 7.1 million cells

The simulation results on all four mesh sizes indicate that as the number of cells increases, accuracy also increases as expected. The difference in results due to the change in the mesh size for static pressure is not significant, however it is not true for the heat transfer results, especially on the leeside; 2.3 million and 3.05 million cell results are nearly identical, but the 5.4 million and 7.1 million cell mesh results are closer to the experiment. It could be argued that in excess of 10 million cells are probably needed to obtain more accurate results. In this study, 3.05 million cells have been used in all the computations.

Chapter 4

Conclusion

The purpose of this study was to validate the building-blocks of CFD methods and obtain best practice guidelines for predicting the flow properties of hypersonic flow over a circular yawed cone. The high quality, structured conical mesh was needed to allow adequate resolution of both the shock layer and the boundary layer while reducing the computing time. Most of the simulation results agreed with Tracy's wind tunnel experiment, except for heat transfer measurements near the leeward meridian. This may be due to insufficient grid resolution between the shock and the cone surface near the leeward side as well as due to the inadequacy of the Spalart-Allmaras (SA) turbulence model for computing high speed flows. Nevertheless, the results show that CFD can be used with acceptable accuracy for computing hypersonic flow over circular yawed cones and perhaps other space vehicles.

4.1 Future Work

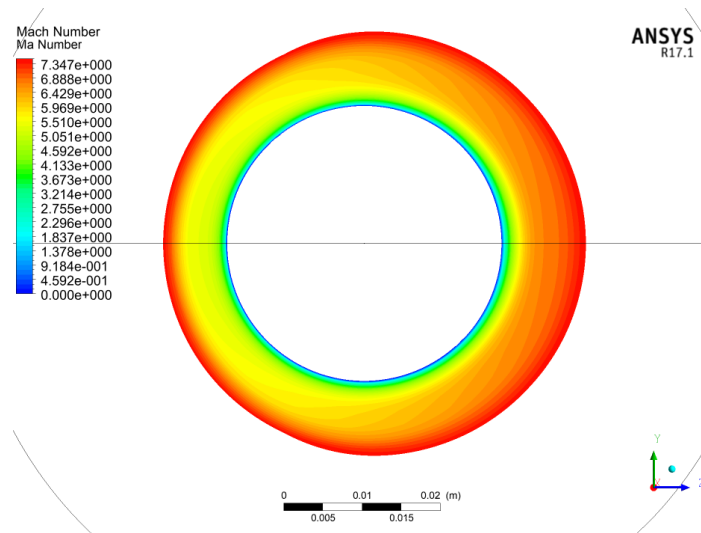
The results described in this thesis could be further improved by examining the effects of different turbulence models. The large discrepancy between the computations and the experiment in the heat transfer coefficient can most likely be attributed to the inadequacy of the SA turbulence model for computing high speed turbulent flows. In addition, additional computations should be performed using the second data set in Tracy's experiment at lower Reynolds numbers. These calculations can be useful in determining the role of turbulence model in the computational accuracy. Finally, the mesh density could be improved by dynamically adapting the grid around the shock layer and boundary layer. This effect was noted in the mesh independence study in chapter 3. Eventually the inclusion of real gas and dissociation effects should be considered in modeling.

Appendix A

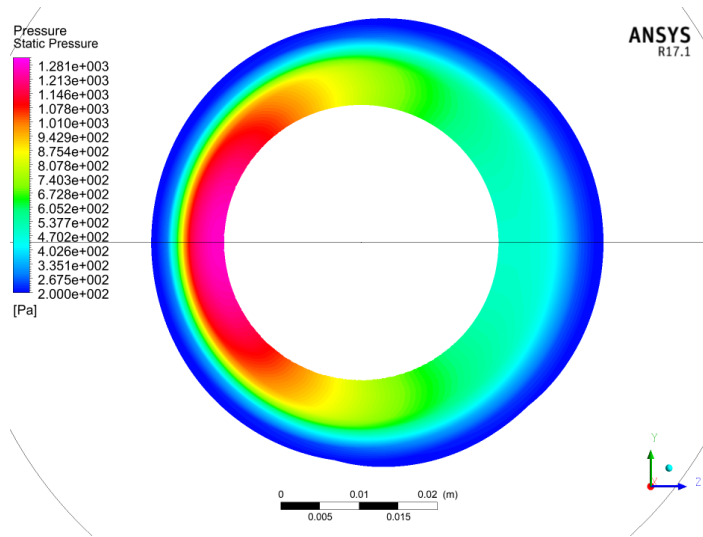
Supplementary Plots

The following figures show the contour plots of Mach number, static pressure, and temperature respectively for cones at various yaw angles. These cross sections are in the circumferential plane 4.0 inches downstream of the cone vertex.

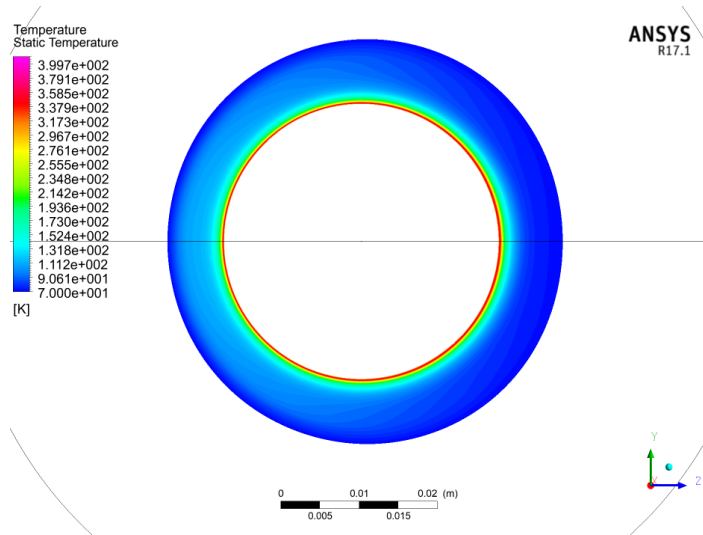
A1: Cone at 4° Angle of Attack



A1.1 Cone at 4° yaw, Mach Number Contours

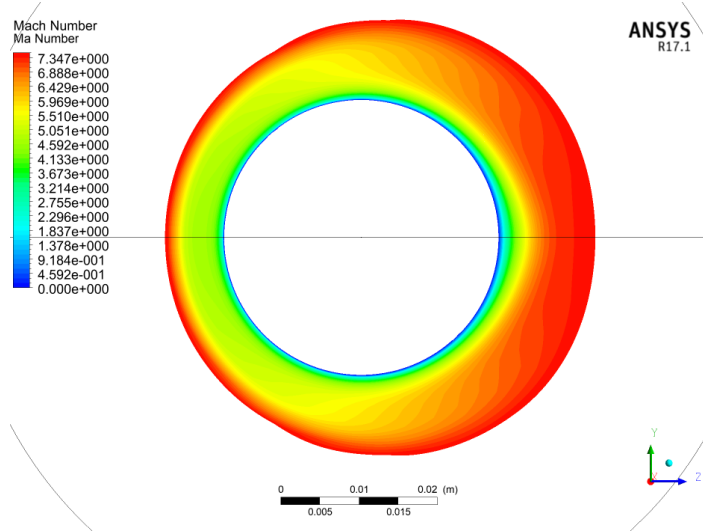


A1.2 Cone at 4° yaw, Static Pressure Contours

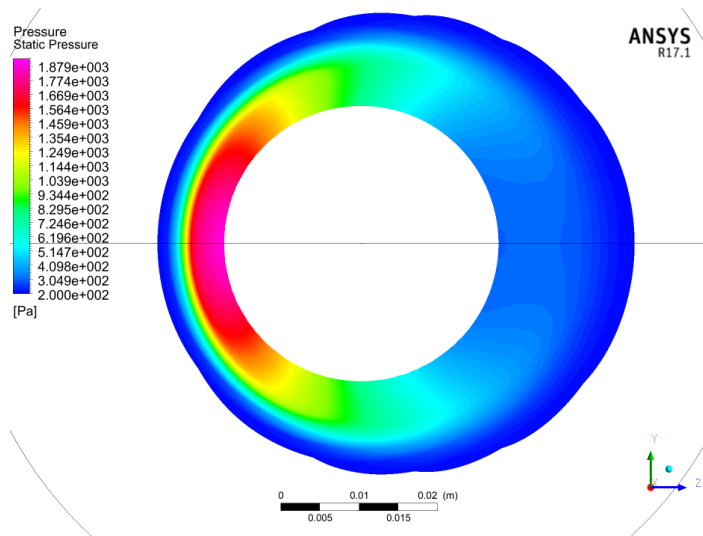


A1.3 Cone at 4° yaw, Static Temperature Contours

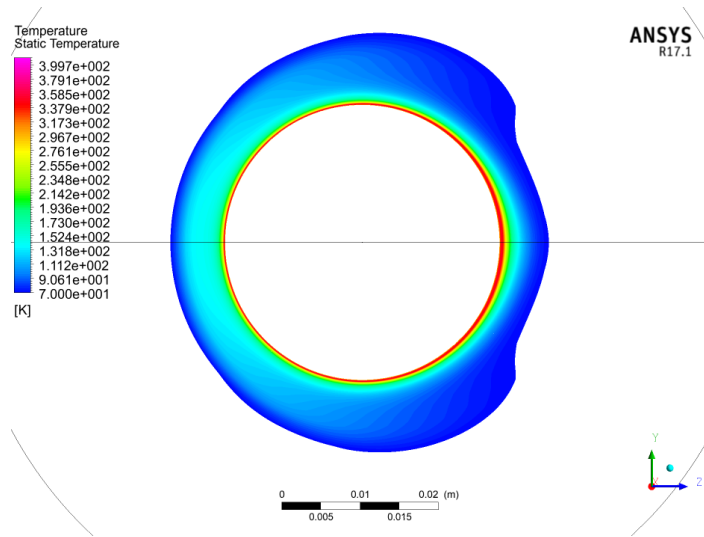
A2: Cone at 8° Angle of Attack



A2.1 Cone at 8° yaw, Mach Number Contours

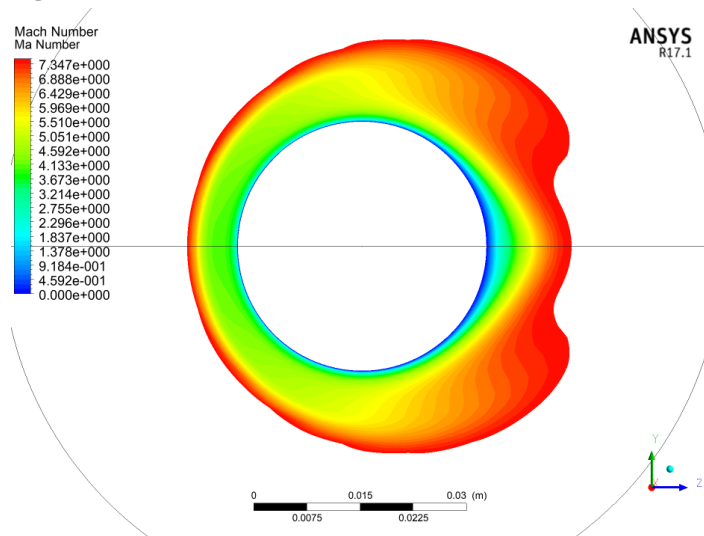


A2.2 Cone at 8° yaw, Static Pressure Contours

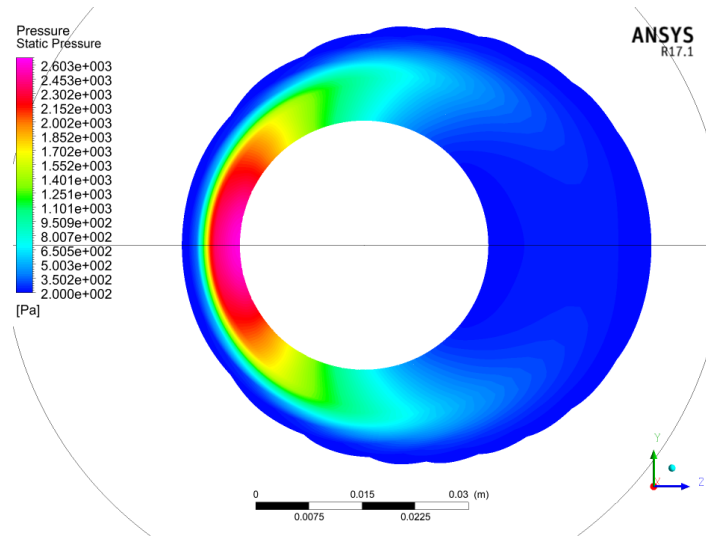


A2.3 Cone at 8° yaw, Static Temperature Contours

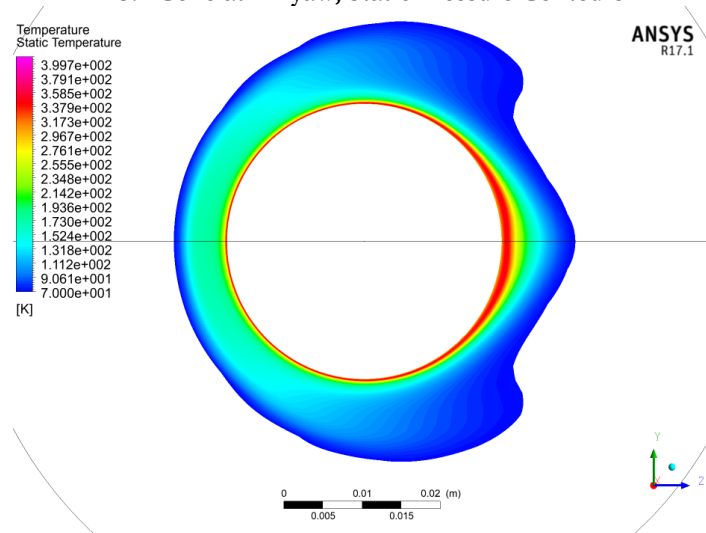
A3: Cone at 12° Angle of Attack



A3.1 Cone at 12° yaw, Mach Number Contours

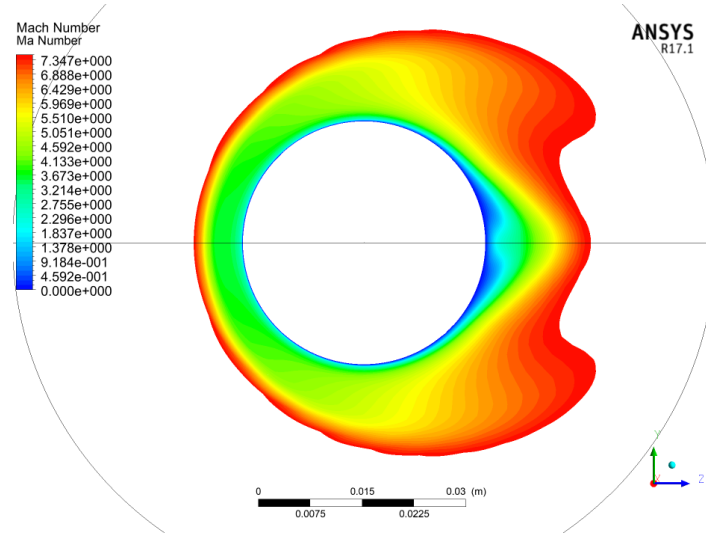


A3.2 Cone at 12° yaw, Static Pressure Contours

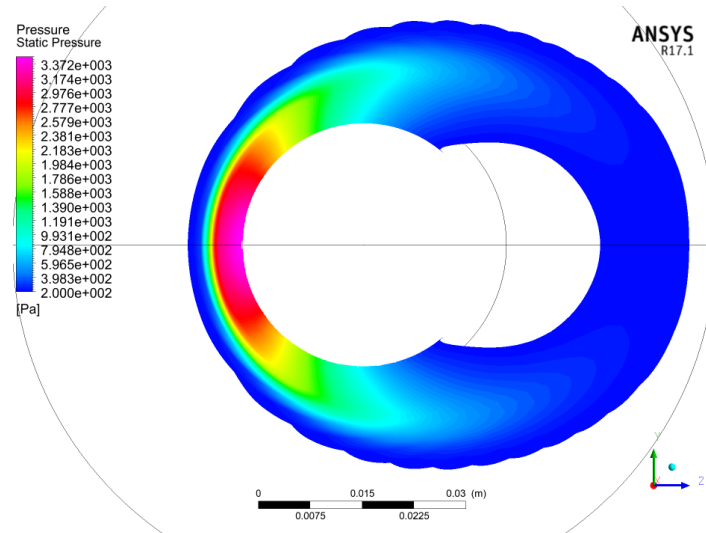


A3.3 Cone at 12° yaw, Static Temperature Contours

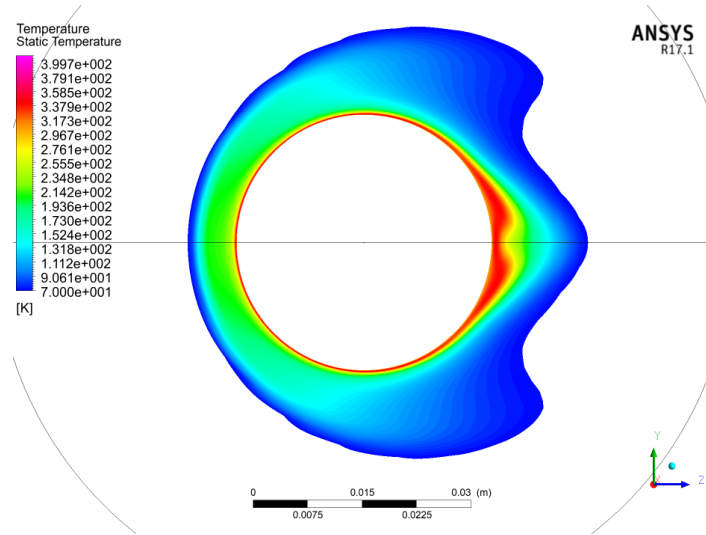
A4: Cone at 16° Angle of Attack



A4.1 Cone at 16° yaw, Mach Number Contours

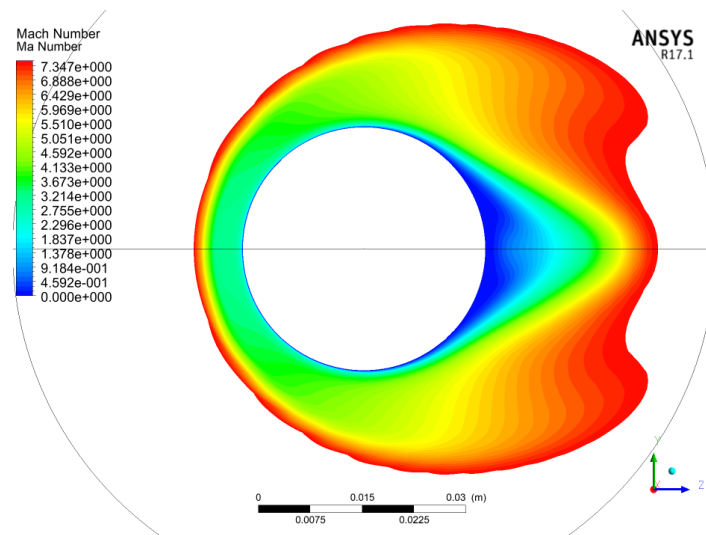


A4.2 Cone at 16° yaw, Static Pressure Contours

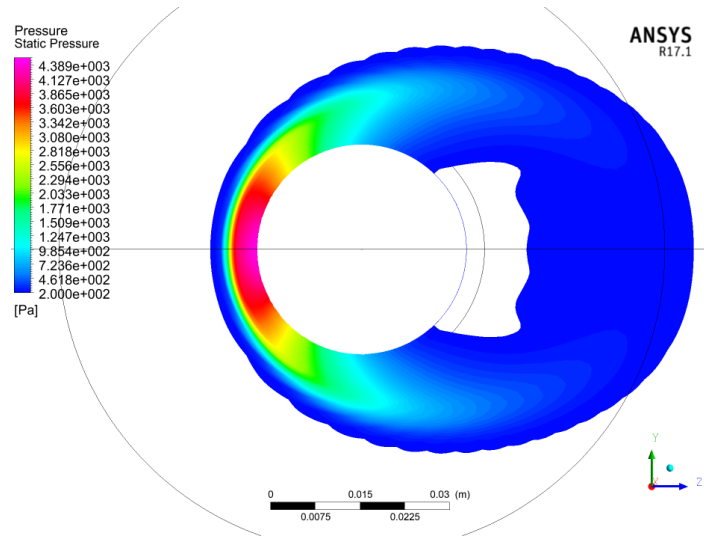


A4.3 Cone at 16° yaw, Static Temperature Contours

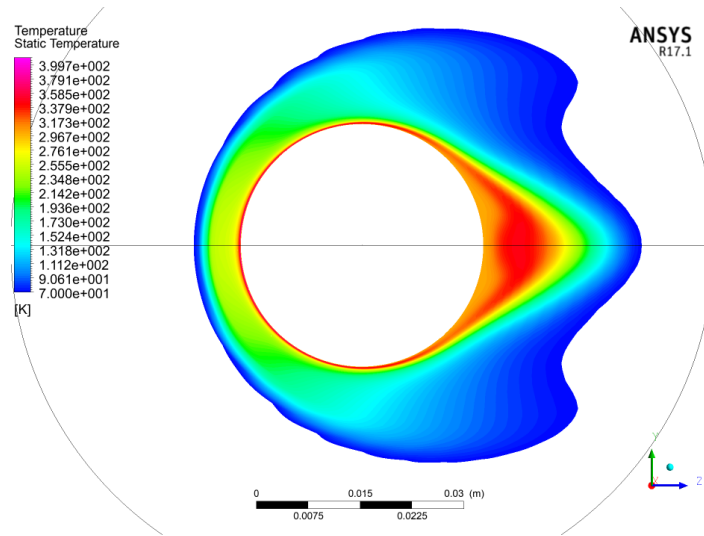
A5: Cone at 20° Angle of Attack



A5.1 Cone at 16° yaw, Mach Number Contours



A5.2 Cone at 20° yaw, Static Pressure Contours



A5.3 Cone at 20° yaw, Static Temperature Contours

Appendix B

Computer Specifications

Simulations were run on the custom desktop computer with specifications given in Table 2.

Table 2: Computer Hardware Used in Simulations

Component	Manufacturer	Model
CPU	Intel	(2) Xeon E5-2690 V1 2.9 MHz
Motherboard	SuperMicro	MBD-X9Dai-O EATX
RAM	Kingston	64 GB DDR3-1600 MHz
GPU	NVIDIA	Quadro K4200 4GB

With the above hardware, each simulation converged after an average of 22,000 iterations at a rate of 203.7 iterations per hour.

References

- [1] R. S. Bartlett, "Tables of Supersonic Symmetrical Flow around Right Circular Cones, with and without the Addition of Heat at the Wave," Ministry of Technology Aeronautical Research Council, London, 1968.
- [2] Z. Kopal, "Tables of Supersonic Flow Around Yawing Cones," Massachusetts Institute of Technology Department of Electrical Engineering, Cambridge, 1947.
- [3] A. Ferri, "Supersonic Flow Around Circular Cones at Angles of Attack," National Advisory Committee for Aeronautics, Langley Field VA, 1950.
- [4] I. Sapunkov, "Hypersonic Flow Past a Circular Cone at An Angle of Attack," *PMM*, vol. 27, no. 5, pp. 930-939, 1963.
- [5] J. N. Moss, G. J. LeBeau and C. E. Glass, "Hypersonic Shock Interactions About a 25/65 Sharp Double Cone," *Rarified Gas Dynamics: 23rd International Symposium*, pp. 425-432, 2003.
- [6] R. Gosse and R. Kimmel, "CFD Study of Three-Dimensional Hypersonic Laminar Boundary Layer Transition on a Mach 8 Elliptic Cone," *American Institute of Aeronautics and Astronautics*, 2009.
- [7] R. R. Tracy, "Hypersonic Flow over a Yawed Circular Cone," Graduate Aeronautical Laboratories California Institute of Technology, Pasadena, California, 1963.
- [8] J. W. Maccoll, "The Conical Shock Wave formed by a Cone Moving at a High Speed," *Proceedings of the Royal Society of London. Series A, Mathematical and Physical Sciences, Vol. 159, No. 898*, pp. 459-472, 1937.
- [9] B. Jones, "Viscous Grid Spacing Calculator," 3 July 1997. [Online]. Available: <https://geolab.larc.nasa.gov/APPS/YPlus/>.
- [10] W. Sutherland, "The Viscosity of Gases and Molecular Force," *Philosophical Magazine, S 5,36*, pp. 507-531, 1893.
- [11] N. Hall, "Isentropic Flow Relations," NASA Glenn Research Center, 5 May 2015. [Online]. Available: <https://www.grc.nasa.gov/www/k-12/airplane/isentrop.html>.
- [12] "ANSYS FLUENT User Manual 17.0," 18 April 2016. [Online]. Available: https://www.sharcnet.ca/Software/Ansys/17.0/en-us/help/ai_sinfo/flu_intro.html.
- [13] T. L. Bergman, A. S. Lavine, F. P. Incropera and D. P. Dewitt, *Fundamentals of Heat and Mass Transfer*, John Wiley & Sons, Inc., 2011.
- [14] G. V. Candler, I. Nompelis and M.-C. Druguet, "CFD Validation for Hypersonic Flight: Hypersonic Double-Cone Flow Simulations," *American Institute of Aeronautics & Astronautics*, no. RTO-TR-AVT-007-V3, 2002.

- [15] P. A. Gnoffo, "Computational Fluid Dynamics Technology For Hypersonic Applications," NASA Langley Research Center, Hampton VA, 2004.

Vita

Julian Dallas Cecil

Degrees

M.S. Aerospace Engineering, May 2018
B.S. Mechanical Engineering, May 2018
B.S. Applied Mathematics, May 2014

**Professional
Societies**

Society of Automotive Engineers

May 2018